

SCIENTIFIC REPORTS

OPEN

Strain-stress study of $\text{Al}_x\text{Ga}_{1-x}\text{N}/\text{AlN}$ heterostructures on *c*-plane sapphire and related optical properties

Yining Feng^{1,2}, Vishal Saravade³, Ting-Fung Chung¹, Yongqi Dong^{4,5}, Hua Zhou⁵, Bahadir Kucukgok^{1,2}, Ian T. Ferguson^{3,6} & Na Lu^{1,7}

This work presents a systematic study of stress and strain of $\text{Al}_x\text{Ga}_{1-x}\text{N}/\text{AlN}$ with composition ranging from GaN to AlN, grown on a *c*-plane sapphire by metal-organic chemical vapor deposition, using synchrotron radiation high-resolution X-ray diffraction and reciprocal space mapping. The *c*-plane of the $\text{Al}_x\text{Ga}_{1-x}\text{N}$ epitaxial layers exhibits compressive strain, while the *a*-plane exhibits tensile strain. The biaxial stress and strain are found to increase with increasing Al composition, although the lattice mismatch between the $\text{Al}_x\text{Ga}_{1-x}\text{N}$ and the buffer layer AlN gets smaller. A reduction in the lateral coherence lengths and an increase in the edge and screw dislocations are seen as the $\text{Al}_x\text{Ga}_{1-x}\text{N}$ composition is varied from GaN to AlN, exhibiting a clear dependence of the crystal properties of $\text{Al}_x\text{Ga}_{1-x}\text{N}$ on the Al content. The bandgap of the epitaxial layers is slightly lower than predicted value due to a larger tensile strain effect on the *a*-axis compared to the compressive strain on the *c*-axis. Raman characteristics of the $\text{Al}_x\text{Ga}_{1-x}\text{N}$ samples exhibit a shift in the phonon peaks with the Al composition. The effect of strain on the optical phonon energies of the epitaxial layers is also discussed.

III-Nitride alloys have attracted considerable attention in a wide range of applications of optical, optoelectronic, high-power, and high-frequency devices such as light emitting diodes (LEDs), laser diodes, and high electron mobility transistors (HEMTs)^{1–6}. For instance, the hexagonal $\text{Al}_x\text{Ga}_{1-x}\text{N}$ is one of the most promising candidates for ultraviolet (UV)-LED applications, especially because of its wide bandgap (E_g) range from 3.42 eV (for GaN) to 6.2 eV (for AlN) at room temperature⁷. $\text{Al}_x\text{Ga}_{1-x}\text{N}$ is also an optimum intermediate layer for InGaN-based LEDs and InAlN transistors^{2,8–10}. $\text{Al}_x\text{Ga}_{1-x}\text{N}/\text{GaN}$ HEMTs paves the way for achieving high power radio frequency (RF) devices due to high electron mobility, large critical breakdown field, high sheet charge density, high electron saturation velocity, and high temperature operation¹¹. $\text{Al}_x\text{Ga}_{1-x}\text{N}/\text{AlN}$ heterostructure combines the photodetector abilities of deep ultra-violet (DUV) AlN along with the tunable bandgap $\text{Al}_x\text{Ga}_{1-x}\text{N}$, thereby also suppressing the visible spectrum and enhancing the UV/visible rejection ratio^{12,13}. This has applications in military target or missile detection, biochemical sensing, as solar-blind detectors, air/water purification, curing, and biomedical therapies and instrumentation^{14–17}. Considering the photodetector applications, AlN has a higher bandgap than $\text{Al}_x\text{Ga}_{1-x}\text{N}$ and hence the resulting photodetector spectrum (of light waves incident on $\text{Al}_x\text{Ga}_{1-x}\text{N}$ surface) would be dominantly dependent on the $\text{Al}_x\text{Ga}_{1-x}\text{N}$ epitaxial layer properties; as opposed to other structures consisting of $\text{Al}_x\text{Ga}_{1-x}\text{N}$ and a lower bandgap material, where it could be difficult to separate the effects of the two materials on the energy spectrum. Also, an $\text{Al}_x\text{Ga}_{1-x}\text{N}/\text{AlN}$ structure would have the flexibility to function as a photodetector from top and bottom sides with front and back illumination respectively, with the top $\text{Al}_x\text{Ga}_{1-x}\text{N}$ epitaxial layer having bandgap range from ~4 eV to ~6 eV depending on the Al content, and a bottom

¹Lyles School of Civil Engineering, Birck Nanotechnology Center, Purdue University, West Lafayette, IN, 47907, USA.

²Applied Materials Division, Argonne National Laboratory, 9700 South Cass Ave, Lemont, IL, 60439, USA. ³Electrical and Computer Engineering, Missouri University of Science and Technology, Rolla, MO, 65409, USA. ⁴National Synchrotron Radiation Laboratory, University of Science and Technology of China, Hefei, Anhui, 230026, China.

⁵Advanced Photon Source, Argonne National Laboratory, 9700 South Cass Ave, Lemont, IL, 60439, USA. ⁶Southern Polytechnic College of Engineering and Engineering Technology, Kennesaw State University, Marietta, GA, 30060, USA. ⁷School of Materials Engineering, Purdue University, West Lafayette, IN, 47907, USA. Correspondence and requests for materials should be addressed to I.T.F. (email: ianf@mst.edu) or N.L. (email: luna@purdue.edu)

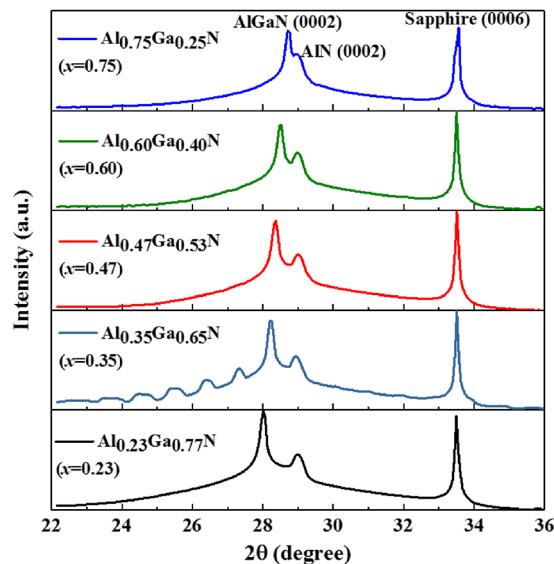


Figure 1. HRXRD $2\theta-\omega$ scan near (0002) Bragg reflection plane for the $\text{Al}_x\text{Ga}_{1-x}\text{N}$ thin films.

AlN layer with 6.2 eV band gap. Using an AlN intermediate layer for $\text{Al}_x\text{Ga}_{1-x}\text{N}$ could also improve the crystal quality of the heterostructure and reduce absorption losses¹⁶. However, highly efficient and reliable electronic and optoelectronic devices require epitaxial layers with excellent crystal quality (i.e., low dislocation density and residual strain). It is challenging to grow high-quality $\text{Al}_x\text{Ga}_{1-x}\text{N}$ thin films, particularly with high Al composition (x); this is due to the lattice mismatch and thermal expansion difference between the thin films and substrates, which generally results in high-level strain-stress and mosaicity^{18–20}. Strain-stress in epitaxial layers is one of the leading factors that reduces the electron mobility and degrades the device performance^{21–23}. Also, their optical and morphological properties could be improved by reducing the strain and stress. Therefore, it is vital to understand the strain and stress mechanism for improving the optical and electronic properties and applications of III-Nitrides.

High-resolution X-ray diffraction (HRXRD) and reciprocal space mapping (RSM) could be used to understand the crystal properties and to analyze the strain and stress in epitaxially grown III-Nitride films²⁴. The effect of different intermediate layers such as AlN, GaN, and step-graded $\text{Al}_x\text{Ga}_{1-x}\text{N}$ for $\text{Al}_x\text{Ga}_{1-x}\text{N}/\text{GaN}$ HEMT structures on silicon (111) substrate has been studied by XRD, RSM and Hall effect measurements, showing that the in-plane stress can largely affect the two-dimensional electron gas mobility and carrier concentration²⁵.

The origin of stresses in $\text{Al}_x\text{Ga}_{1-x}\text{N}/\text{GaN}$ heterostructures grown on c -plane sapphire substrate relies mainly on the thickness and growth temperature of the layers, alloy composition, device structure, and doping^{20,23,26–28}. In the case of $\text{Al}_{0.4}\text{Ga}_{0.6}\text{N}/\text{AlN}/\text{GaN}$ (superlattices)/GaN/sapphire and $\text{Al}_{0.6}\text{Ga}_{0.4}\text{N}/\text{AlN}/\text{sapphire}$, stress was released due to misfit dislocations at several interfaces in the heterostructure due to composition pulling effect²⁹. Also, strain and threading dislocations accumulation increased at step edges in Λ -shape distributed $\text{Al}_x\text{Ga}_{1-x}\text{N}$ (x from 7% to 30%) grown on AlN/GaN/sapphire substrates³⁰. In the case of a GaN/ $\text{Al}_x\text{Ga}_{1-x}\text{N}$ (graded x from 0 to 26 and 42%)/GaN/sapphire structure, a tensile strain was observed in the $\text{Al}_x\text{Ga}_{1-x}\text{N}$ and a compressive strain in the GaN cap layer; also, crystal coherence was broken at the interfaces but it was consistent within the $\text{Al}_x\text{Ga}_{1-x}\text{N}$ layers³¹. Crystal defects and dislocations could be attenuated by growing a high temperature (HT) AlN intermediate layer as reported in the case of $\text{Al}_x\text{Ga}_{1-x}\text{N}/\text{AlN}$ (HT)/GaN/sapphire³² and by modifying or reducing the interfaces.

However, a systematic study of strain and stress in $\text{Al}_x\text{Ga}_{1-x}\text{N}/\text{AlN}$ heterostructures, especially for high x (>0.5) $\text{Al}_x\text{Ga}_{1-x}\text{N}$ epitaxial layers, on c -plane sapphire substrates by synchrotron radiation HRXRD and RSM technique has not been reported. It is crucial to study the crystal properties of $\text{Al}_x\text{Ga}_{1-x}\text{N}/\text{AlN}$ structures, which is a step towards improving their quality and potential for practical applications.

In this work, the overall strain, biaxial strain, hydrostatic strain, and biaxial stress along the a - and c -axis, are analyzed and calculated for $\text{Al}_x\text{Ga}_{1-x}\text{N}/\text{AlN}$ heterostructure on sapphire substrates with varying x and $\text{Al}_x\text{Ga}_{1-x}\text{N}$ composition from GaN to AlN using synchrotron radiation HRXRD and RSM. The epitaxial layers have a good surface quality and are free of cracks. The effect of the Al content on the crystal properties, dislocation densities and coherence lengths are discussed. The effect of strain on the optical properties of the $\text{Al}_x\text{Ga}_{1-x}\text{N}$ thin films has been investigated using photoluminescence (PL) and Raman spectroscopy.

Results and Discussion

The crystal structure and lattice parameters of MOCVD-grown $\text{Al}_x\text{Ga}_{1-x}\text{N}$ and AlN have been studied using HRXRD and RSM techniques, while photoluminescence and Raman measurement results are discussed to understand the bandgap and phonon modes in $\text{Al}_x\text{Ga}_{1-x}\text{N}$ and AlN. Figure 1 shows the $2\theta-\omega$ Bragg reflections ($\lambda = 1.23984 \text{ \AA}$) around (0002) crystal planes for $\text{Al}_x\text{Ga}_{1-x}\text{N}$ with varying x . The effect of strain is taken into account to determine the x values as per the synchrotron radiation HRXRD results³³. Bragg reflection peaks of (0002) from $\text{Al}_x\text{Ga}_{1-x}\text{N}$ and AlN, and of (0006) from the sapphire substrate, are observed. The satellite peaks or the Laue oscillations in $\text{Al}_{0.35}\text{Ga}_{0.65}\text{N}$ could be due to relatively smoother surface of $\text{Al}_x\text{Ga}_{1-x}\text{N}$ with 35% Al or

Al composition (x)	In-plane lattice parameter [Å]		Out-of-plane lattice parameter [Å]		Elastic constant [GPa]				Poisson ratio (ν)
	Calculated (a)	Unstrained (a ₀)	Calculated (c)	Unstrained (c ₀)	C ₁₁	C ₁₂	C ₁₃	C ₃₃	
x = 0.23	3.190	3.171	5.121	5.138	394.83	145.92	104.39	395.93	0.203
x = 0.47	3.185	3.152	5.061	5.088	399.87	146.88	102.71	393.77	0.204
x = 0.75	3.169	3.130	4.998	5.031	405.75	148.00	100.75	391.25	0.205

Table 1. Calculated strained (*a*, *c*) parameters (from HRXRD 2θ–ω scan and asymmetric RSM scans) and unstrained lattice parameters (*a*₀, *c*₀) (from Vegard's law), Al composition (*x*)³³, elastic constants (*C*₁₁, *C*₁₂, *C*₁₃, and *C*₃₃) and Poisson ratio (*ν*) of Al_xGa_{1–x}N. (ν₀^{AlN} = 0.207 and ν₀^{GaN} = 0.202)

due to the scattering of x-rays within the Al_{0.35}Ga_{0.65}N and the AlN layers. However, the primary goal here is to investigate the effect of Al content on the dominant and defining (0002) peak in the epitaxial layers.

The out-of-plane *c*-axis lattice constant (*c*) of Al_xGa_{1–x}N thin films were calculated as shown in Table 1. Vegard's law provides reliable unstrained lattice constants (*c*₀, *a*₀) for Al_xGa_{1–x}N films using the bandgaps of GaN and AlN, and considering the very small lattice mismatch (~2%) between GaN and AlN^{19,33–36}. The calculated *c*, is lower than the unstrained *c*₀, indicating a compressive strain along the *c*-axis (out-of-plane) in the Al_xGa_{1–x}N thin films.

RSM based analysis were also done to determine the lattice constants and the stress-strain phenomenon in Al_xGa_{1–x}N with changes in *x*. Figure 2 shows the symmetric plane RSM in the (0002) direction. A clear broadening of Al_xGa_{1–x}N reciprocal lattice points (RLPs) reflection intensity distribution towards *Q*_z and *Q*_x is seen. It can be observed that the maximum reflection intensity of Al_xGa_{1–x}N shifts to higher *Q*_z values and the lattice constant *c* reduces, as *x* increases, which agrees very well with the results obtained from the 2θ–ω scan. Also, broadening along the *Q*_z direction increases with *x*. Changes in the RSM plots with different Al content seem to be dominated by the Al_xGa_{1–x}N layer.

Reciprocal space map around the AlN asymmetric (10 $\bar{1}$ 3) RLP is illustrated in Figure 3. Based on the information from the asymmetric RSM scan, lattice parameters (*a* and *c*) were calculated for the hexagonal structure Eq. (1)^{37–39}:

$$a = \frac{2\pi}{|Q_x|} \sqrt{\frac{4(h^2 + k^2 + hk)}{3}}, \quad c = \frac{2\pi l}{Q_z}, \quad (1)$$

Table 1 presents the calculated lattice parameters from the asymmetric RSM measurement (in this particular case, *h* = 1, *k* = 0, and *l* = 3) for Al_xGa_{1–x}N. The calculated *c* from asymmetric RSMs is very close to the one obtained by HRXRD 2θ–ω scans for each sample, with a difference of about 0.06%; hence only the *c*-parameters from the HRXRD results are shown. The calculated *a* is larger than the unstrained one (*a*₀) obtained by Vegard's law, which is due to the tensile strain along the *a*-axis (in-plane) in the Al_xGa_{1–x}N epitaxial layers. Also, the *a*-lattice constant reduces with an increase in *x*, similar to *c*. A reduction in the lattice size and increase in the strain is seen in Al_xGa_{1–x}N with an increase in the Al content in the alloy.

Figure 3 shows that with increasing Al composition, the maximum reflection intensity of Al_xGa_{1–x}N RLPs progressively shifts from a partially relaxed (*R* = 1) towards a fully strained (*R* = 0) position. Since the AlN layer is thinner (~120 nm) than the Al_xGa_{1–x}N layer (~800 nm), its reflection peak intensity is lower than Al_xGa_{1–x}N. The intensity of Al_xGa_{1–x}N RLP broadens along the direction associated with the relaxation of the layer (the dashed black line). The Al_xGa_{1–x}N RLPs get closer to the fully strained position with an increase in *x*. Note that both AlN and Al_{0.75}Ga_{0.25}N have a similar *Q*_x value of –2.38 Å^{–1}. An increase in the strain is observed with Al incorporation in Al_xGa_{1–x}N, despite of reductions in lattice mismatch. As seen in Figure 3, a strain complementary to Al_xGa_{1–x}N is induced in the AlN intermediate layer which increases with *x* as the Al_xGa_{1–x}N layer is relaxed and adds to the inherent strain that is already present in AlN. The broadening in the symmetric and asymmetric RLPs implies an increase in the screw and edge dislocations (which are in the order of 10⁸–10⁹ cm^{–2}) respectively with *x*. The RSM and the 2θ–ω results show that the dislocations and the coherence lengths in Al_xGa_{1–x}N/AlN change with *x*. Lattice constants of hexagonal AlN are typically smaller than GaN and hence, a reduction in the lateral correlation lengths and an increase in the dislocations are seen as the Al_xGa_{1–x}N composition is varied from GaN to AlN.

The overall in-plane strain (ϵ_a) and out-of-plane strain (ϵ_c) in the Al_xGa_{1–x}N layers were determined using Eq. (2)^{38,40–42}:

$$\epsilon_a = \frac{a - a_0}{a_0}, \quad \epsilon_c = \frac{c - c_0}{c_0}, \quad (2)$$

The calculated strains (ϵ_a and ϵ_c) are attributed to the biaxial (ϵ_a^b and ϵ_c^b) and hydrostatic (ϵ_h) strains as shown in Eq. (3)^{34,36}. (ϵ_a^b and ϵ_c^b are the biaxial strains along *a*- and *c*-directions, respectively.)

$$\epsilon_a = \epsilon_a^b + \epsilon_h, \quad \epsilon_c = \epsilon_c^b + \epsilon_h, \quad (3)$$

where ϵ_h is defined as $\epsilon_h = \frac{1-\nu}{1+\nu} \left(\epsilon_c + \frac{2\nu}{1-\nu} \right)$, ν is Poisson's ratio of Al_xGa_{1–x}N calculated using Vegard's law ($\nu_{AlGaN}(x) = x_{AlN} + (1-x)_{GaN}$)⁴³ and shown in Table 1. For the hexagonal crystal structure, the in-plane biaxial stress (σ^b) in the Al_xGa_{1–x}N epitaxial layer can be determined by $\sigma^b = M_b \epsilon_a^b$, where M_b is the biaxial elastic modulus given by $M_b = \left(C_{11} + C_{12} + 2\frac{C_{13}^2}{C_{33}} \right)$ ⁴¹. The elastic constants (*C*_{*ij*}) of Al_xGa_{1–x}N (Table 1) can be obtained by

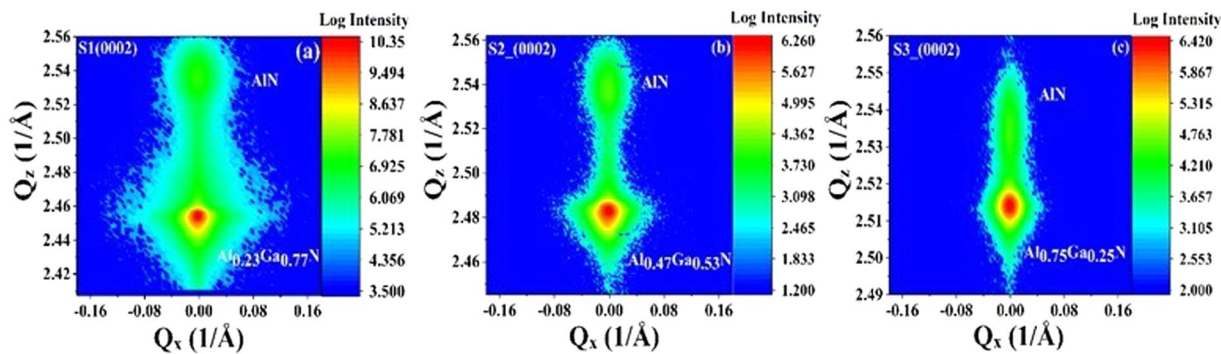


Figure 2. Symmetric RSM (0002) scan of the $\text{Al}_x\text{Ga}_{1-x}\text{N}/\text{AlN}$ thin films.

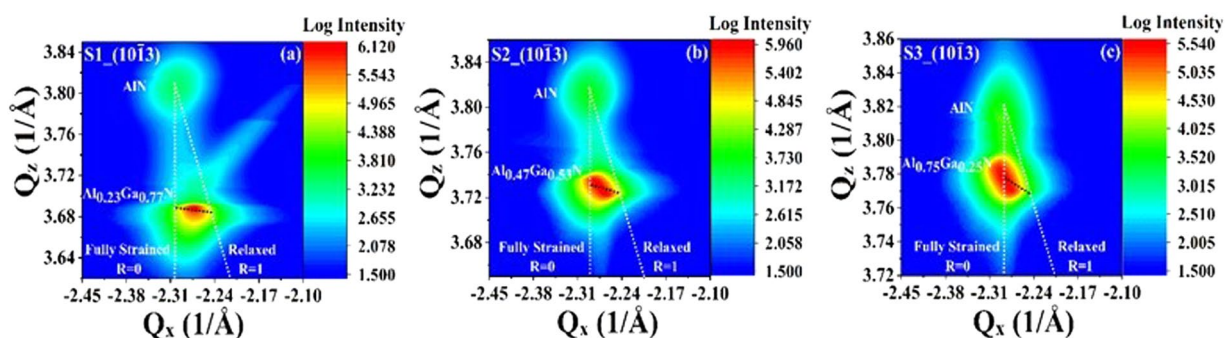


Figure 3. Asymmetric RSM ($10\bar{1}3$) scan of the $\text{Al}_x\text{Ga}_{1-x}\text{N}/\text{AlN}$ thin films grown on sapphire. (a) $\text{Al}_{0.23}\text{Ga}_{0.77}\text{N}$, (b) $\text{Al}_{0.47}\text{Ga}_{0.53}\text{N}$, and (c) $\text{Al}_{0.75}\text{Ga}_{0.25}\text{N}$. The dashed white lines indicate where the fully relaxed ($R = 1$) and fully strained ($R = 0$) $\text{Al}_x\text{Ga}_{1-x}\text{N}$ layers with varying Al compositions should be. The dashed black lines show the relaxation directions in the reciprocal space for different Al compositions.

Al composition (x)	In-plane strain (ϵ_a) [%]	In-plane biaxial strain (ϵ_a^b) [%]	Out-of-plane strain (ϵ_c) [%]	Out-of-plane biaxial strain (ϵ_c^b) [%]	Hydrostatic strain (ϵ_h)	Biaxial stress (σ^b) [GPa]
$x = 0.23$	0.6	0.6	-0.3	-0.3	1.06×10^{-6}	2.9
$x = 0.47$	1.0	1.0	-0.5	-0.5	-2.35×10^{-5}	5.1
$x = 0.75$	1.2	1.2	-0.6	-0.6	-3.50×10^{-6}	6.3

Table 2. Measured in-plane and out-of-plane strains, biaxial strains, hydrostatic strain, and biaxial stress of $\text{Al}_x\text{Ga}_{1-x}\text{N}$. Positive and negative values denote tensile and compressive strains respectively.

Vegard's law ($C_{ij}^{\text{AlGa}}(x) = xC_{ij}^{\text{AlN}} + (1-x)C_{ij}^{\text{GaN}}$)^{44,45}. The calculated strains, biaxial strains, hydrostatic strain, and biaxial stress for $\text{Al}_x\text{Ga}_{1-x}\text{N}$ epitaxial layers are summarized in Table 2. It can be seen that the in-plane (biaxial) strains are tensile, while the out-of-plane (biaxial) strains are compressive because of the different lattice mismatch along the in-plane and out-of-plane axes¹⁹ as also seen in the HRXRD results.

The biaxial strain has values close to the total strain in $\text{Al}_x\text{Ga}_{1-x}\text{N}$ due to the relatively smaller values of ϵ_h and very few impurities introduced during growth. Also, the full width at half maximum (FWHM) values of the HRXRD (0002) ω scans (not shown here) are found to be 627, 642, and 847 arcsec for $\text{Al}_{0.23}\text{Ga}_{0.77}\text{N}$, $\text{Al}_{0.47}\text{Ga}_{0.53}\text{N}$, and $\text{Al}_{0.75}\text{Ga}_{0.25}\text{N}$, respectively (Table 3)³². The lateral coherence lengths would range from 100 nm to 200 nm and have inverse proportionality with the Al content, indicating that the $\text{Al}_x\text{Ga}_{1-x}\text{N}$ samples used in this study are of good crystal quality.

The broadening of the FWHM of (0002) HRXRD ω scans in $\text{Al}_x\text{Ga}_{1-x}\text{N}$ could be associated with the screw (c -type) threading dislocation (TD) along the c -axis. Figure 4(a) presents the compositional dependence of screw (c -type) TD density and out-of-plane strain in the $\text{Al}_x\text{Ga}_{1-x}\text{N}$ thin films. The dislocation density of the $\text{Al}_x\text{Ga}_{1-x}\text{N}$ thin films can be estimated from:

$$D_{\text{screw}} = \frac{\beta_{(0002)}^2}{4.35b_{\text{screw}}^2}, \quad (4)$$

where D_{screw} is the screw type TD²⁴, β is the FWHM of the (0002) ω scan, and $b_{\text{screw}} = 5.1855 \text{ \AA}$ is the Burgers vector length for screw-type TD. As x increases, both the screw type TD density and the strain increase (Fig. 4(a)).

Al composition (x)	FWHM of HRXRD [arcsec]	Screw TD Density [cm^{-2}]	FWHM of PL [meV]	Energy gap [eV]
$x=0.23$	627	7.9×10^8	74	3.88
$x=0.47$	642	8.3×10^8	100	4.27
$x=0.75$	847	1.4×10^9	206	5.25

Table 3. Summary of structural and optical results of the $\text{Al}_x\text{Ga}_{1-x}\text{N}$ thin films.

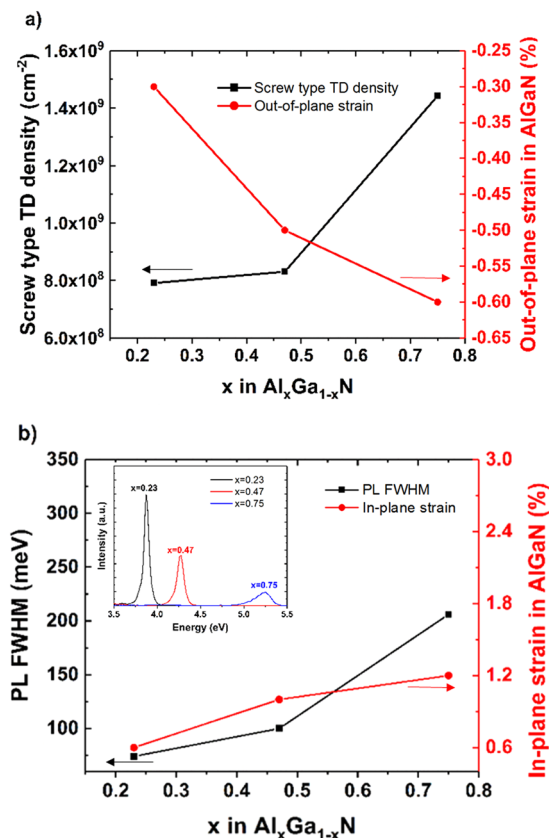


Figure 4. Compositional dependence of (a) screw (c -type) TD density and out-of-plane strain, (b) PL FWHM and in-plane strain of $\text{Al}_x\text{Ga}_{1-x}\text{N}$ layers. The inset shows the room temperature PL spectra of $\text{Al}_{0.23}\text{Ga}_{0.77}\text{N}$, $\text{Al}_{0.47}\text{Ga}_{0.53}\text{N}$, and $\text{Al}_{0.75}\text{Ga}_{0.25}\text{N}$.

Evidently, the high density of screw dislocation observed in the Al-rich samples originated from a compressive strain along the c -axis (up to 0.6%) and a biaxial stress (up to 6.313 GPa), in $\text{Al}_x\text{Ga}_{1-x}\text{N}$, as presented in Table 3.

Photoluminescence measurements (Figure 4(b)) further indicate and help to understand the strain and stress in the epitaxial layers. A broadening of the $\text{Al}_x\text{Ga}_{1-x}\text{N}$ peaks is observed with an increase in x . Also, there is a shift in the peak positions compared to the unstrained energy gaps that are predicted by Vegard's law. The PL peak positions are measured at 3.88, 4.27, and 5.25 eV for $\text{Al}_{0.23}\text{Ga}_{0.77}\text{N}$, $\text{Al}_{0.47}\text{Ga}_{0.53}\text{N}$, and $\text{Al}_{0.75}\text{Ga}_{0.25}\text{N}$, respectively. According to Vegard's law, the predicted energy gap values for $x = 0.23, 0.47,$ and 0.75 are 4.06, 4.73, and 5.51 eV respectively (considering $E_g(\text{AlN}) = 6.2$ eV, $E_g(\text{GaN}) = 3.42$ eV). If a bowing parameter of 1 eV is taken into consideration⁴⁶, the predicted bandgap values are 3.88, 4.47, and 5.32 eV for $x = 0.23, 0.47,$ and 0.75 , respectively. Smaller bandgap in the measured samples as compared to the predicted values, could be attributed more to the stronger tensile strain effect along the a -axis direction than the c -axis compressive strain ($\varepsilon_a \approx 2\varepsilon_c$) in the $\text{Al}_x\text{Ga}_{1-x}\text{N}$ epitaxial layers and hence, to the overall larger lattice constants of $\text{Al}_x\text{Ga}_{1-x}\text{N}$ epitaxial layers as compared to unstrained $\text{Al}_x\text{Ga}_{1-x}\text{N}$. The difference between the predicted and measured bandgap values is more for $x = 0.47$ and 0.75 than $x = 0.23$ due to more residual strain in $\text{Al}_x\text{Ga}_{1-x}\text{N}$ with high Al composition. Also, the bandgap increases with x as would be expected and seems to be tunable between GaN and AlN. The PL peak broadening, intensity suppression and peak shifts could have multiple origins such as a statistical variation in the composition, Al-induced alloy disorder, strain and dislocations.

Raman spectra of the $\text{Al}_x\text{Ga}_{1-x}\text{N}$ samples under 532 nm excitation are shown in Figure 5. Two-mode behavior for the E_2^{high} phonon⁴⁷ and one-mode behavior for the A_1^{LO} phonon⁴⁸ are seen. Here, E_2^{high} and A_1^{LO} phonon modes correspond to the atomic oscillations in the c -plane (parallel to the a -axis) and along the c -axis, respectively. The phonon peaks exhibit a shift with increasing x . The E_2^{high} (GaN-like) phonon is located at 575, 587, and

at 224 nm) was used to measure the optical properties of the $\text{Al}_x\text{Ga}_{1-x}\text{N}$ thin films. Micro-Raman spectroscopy was performed using a Horiba Jobin-Yvon Xplora confocal Raman spectrometer in a backscattering configuration with a 532 nm excitation laser and a grating of 1800 lines/mm.

Data Availability

The datasets generated during and/or analyzed in the current study are available from the corresponding author on reasonable request.

References

- Lu, N. & Ferguson, I. III-nitrides for energy production: photovoltaic and thermoelectric applications. *Semicond. Sci. Technol.* **28**, 074023 (2013).
- Liu, Z. *et al.* p-InGaN/AlGaIn electron blocking layer for InGaN/GaN blue light-emitting diodes. *Appl. Phys. Lett.* **101**, 261106 (2012).
- Kucukgok, B. *et al.* Structural and optical analyses of $\text{Al}_x\text{Ga}_{1-x}\text{N}$ thin films grown by metal organic chemical vapor deposition. *Jpn. J. Appl. Phys.* **54**, 02BA05 (2015).
- Hurwitz, E. N. *et al.* Thermopower Study of GaN-Based Materials for Next-Generation Thermoelectric Devices and Applications. *J. Electron. Mater.* **40**, 513–517 (2011).
- Li, D., Jiang, K. E., Sun, X. & Guo, A. C. AlGaIn photonics: recent advances in materials and ultraviolet devices. *Adv. Opt. Photonics* **10** (2018).
- Jung, S., Baik, K. H., Ren, F., Pearton, S. J. & Jang, S. AlGaIn/GaN Heterostructure Based Schottky Diode Sensors with ZnO Nanorods for Environmental Ammonia Monitoring Applications. *ECS J. Solid State Sci. Technol.* **7**, Q3020–Q3024 (2018).
- Liu, Z. *et al.* Impurity Resonant States p-type Doping in Wide-Band-Gap Nitrides. *Sci. Rep.* **6**, 19537 (2016).
- Yamada, A. *et al.* Advantages of the AlGaIn spacer in InAlN high-electron-mobility transistors grown using metalorganic vapor phase epitaxy. *Jpn. J. Appl. Phys.* **55**, 05FK03 (2016).
- Chang, J.-Y., Tsai, M.-C. & Kuo, Y.-K. *Advantages of blue InGaIn light-emitting diodes with AlGaIn barriers* (2010).
- Lin, B.-C. *et al.* Advantages of Blue LEDs With Graded-Composition AlGaIn/GaN Superlattice EBL. *IEEE PHOTONICS Technol. Lett.* **25** (2013).
- Choi, S., Heller, E., Dorsey, D., Vetry, R. & Graham, S. The impact of mechanical stress on the degradation of AlGaIn/GaN high electron mobility transistors. *J. Appl. Phys.* **114**, 164501 (2013).
- Li, J. *et al.* 200 nm deep ultraviolet photodetectors based on AlN. *Appl. Phys. Lett.* **89**, 213510 (2006).
- Chen, L.-C., Fu, M.-S. & Huang, I.-L. Metal–Semiconductor–Metal AlN Mid-Ultraviolet Photodetectors Grown by Magnetron Reactive Sputtering Deposition. *Jpn. J. Appl. Phys.* **43**, 3353–3355 (2004).
- Biyikli, N., Aytur, O., Kimukin, I., Tut, T. & Özbay, E. Solar-blind AlGaIn-based Schottky photodiodes with low noise and high detectivity. *Appl. Phys. Lett.* **81**, 3272–3274 (2002).
- Litton, C. W., Schreiber, P. J., Smith, G. A., Dang, T. & Morkoc, H. Design requirements for high-sensitivity UV solar blind imaging detectors based on AlGaIn/GaN photodetector arrays: a review. in (ed. Longshore, R. E.) **4454**, 218 (International Society for Optics and Photonics, 2001).
- Sang, L., Liao, M. & Sumiya, M. A Comprehensive Review of Semiconductor Ultraviolet Photodetectors: From Thin Film to One-Dimensional Nanostructures. *Sensors* **13**, 10482–10518 (2013).
- Wośko, M., Szymański, T., Paszkiewicz, B., Pokryszka, P. & Paszkiewicz, R. MOVPE growth conditions optimization for AlGaIn/GaN/Si heterostructures with SiN and LT-AlN interlayers designed for HEMT applications. *J. Mater. Sci. Mater. Electron.* **30**, 4111–4116 (2019).
- Hearne, S. *et al.* Stress evolution during metalorganic chemical vapor deposition of GaN. *Appl. Phys. Lett.* **74**, 356 (1999).
- Şebnem Çetin, S., Kemal Öztürk, M., Özçelik, S. & Özbay, E. Strain analysis of InGaIn/GaN multi quantum well LED structures. *Cryst. Res. Technol.* **47**, n/a–n/a (2012).
- Liu, Y. *et al.* Composition and temperature dependent optical properties of $\text{Al}_x\text{Ga}_{1-x}\text{N}$ alloy by spectroscopic ellipsometry. *Appl. Surf. Sci.* **421**, 389–396 (2017).
- Keller, S. *et al.* Metalorganic chemical vapor deposition of high mobility AlGaIn/GaN heterostructures. *J. Appl. Phys.* **86**, 5850 (1999).
- Ibbetson, J. P. *et al.* Polarization effects, surface states, and the source of electrons in AlGaIn/GaN heterostructure field effect transistors. *Appl. Phys. Lett.* **77**, 250 (2000).
- Lee, H.-P., Perozek, J., Rosario, L. D. & Bayram, C. Investigation of AlGaIn/GaN high electron mobility transistor structures on 200-mm silicon (111) substrates employing different buffer layer configurations. *Sci. Rep.* **6**, 37588 (2016).
- Moram, M. A. & Vickers, M. E. X-ray diffraction of III-nitrides. *Rep. Prog. Phys.* **72**, 036502 (2009).
- Magalhães, S. *et al.* Validity of Vegard's rule for $\text{Al}_{1-x}\text{In}_x\text{N}$ ($0.08 < x < 0.28$) thin films grown on GaN templates. *J. Phys. D: Appl. Phys.* **50**, 205107 (2017).
- He, C. *et al.* Growth of high quality n-Al_{0.5}Ga_{0.5}N thick films by MOCVD. *Mater. Lett.* **176**, 298–300 (2016).
- Liu, N. *et al.* Point-Defect Distribution and Transformation Near the Surfaces of AlGaIn Films Grown by MOCVD. *J. Phys. Chem. C* **123**, 8865–8870 (2019).
- He, C. *et al.* Effect of stress on the Al composition evolution in AlGaIn grown using metal organic vapor phase epitaxy. *Appl. Phys. Express* **9**, 051001 (2016).
- He, C. *et al.* Mechanism of stress-driven composition evolution during hetero-epitaxy in a ternary AlGaIn system. *Sci. Rep.* **6**, 25124 (2016).
- Kuchuk, A. V. *et al.* Nanoscale Electrostructural Characterization of Compositionally Graded $\text{Al}_x\text{Ga}_{1-x}\text{N}$ Heterostructures on GaN/Sapphire (0001) Substrate. *ACS Appl. Mater. Interfaces* **7**, 23320–23327 (2015).
- Stanchu, H. V. *et al.* Local Strain and Crystalline Defects in GaN/AlGaIn/GaN(0001) Heterostructures Induced by Compositionally Graded AlGaIn Buried Layers. *Cryst. Growth Des.* **19**, 200–210 (2019).
- Xu, Q. *et al.* Structural and optical properties of $\text{Al}_x\text{Ga}_{1-x}\text{N}$ ($0.33 \leq x \leq 0.79$) layers on high-temperature AlN interlayer grown by metal organic chemical vapor deposition. *Superlattices Microstruct.* **101**, 144–151 (2017).
- Angerer, H. *et al.* Determination of the Al mole fraction and the band gap bowing of epitaxial $\text{Al}_x\text{Ga}_{1-x}\text{N}$ films. *Appl. Phys. Lett.* **71**, 1504 (1998).
- Fewster, P. F. *X-Ray Scattering from Semiconductors and Other Materials.*, <https://doi.org/10.1142/8648> (WORLD SCIENTIFIC, 2015).
- Tanaka, M., Nakahata, S., Sogabe, K., Nakata, H. & Tobioka, M. Morphology and X-Ray Diffraction Peak Widths of Aluminum Nitride Single Crystals Prepared by the Sublimation Method. *Jpn. J. Appl. Phys.* **36**, L1062–L1064 (1997).
- Yamaguchi, M. *et al.* Brillouin scattering study of bulk GaN. *J. Appl. Phys.* **85**, 8502 (1999).
- Miao, Z. L. *et al.* Strain effects on $\text{In}_x\text{Al}_{1-x}\text{N}$ crystalline quality grown on GaN templates by metalorganic chemical vapor deposition. *J. Appl. Phys.* **107**, 043515 (2010).
- Pereira, S. *et al.* Strain and composition distributions in wurtzite InGaIn/GaN layers extracted from x-ray reciprocal space mapping. *Appl. Phys. Lett.* **80**, 3913–3915 (2002).

39. Jana, S. K. *et al.* High-resolution X-ray diffraction analysis of $\text{Al}_x\text{Ga}_{1-x}\text{N}/\text{In}_y\text{Ga}_{1-y}\text{N}/\text{GaN}$ on sapphire multilayer structures: Theoretical, simulations, and experimental observations. *J. Appl. Phys.* **115**, 174507 (2014).
40. Wu, M. F. *et al.* Strain in AlGaN layer studied by Rutherford backscattering/channeling and x-ray diffraction. *J. Vac. Sci. Technol. B Microelectron. Nanom. Struct. Process. Meas. Phenom.* **17**, 1502 (1999).
41. Harutyunyan, V. S. *et al.* High-resolution x-ray diffraction strain-stress analysis of GaN/sapphire heterostructures. *J. Phys. D. Appl. Phys.* **34**, A35–A39 (2001).
42. Liu, H. F. *et al.* Influence of stress on structural properties of AlGaN/GaN high electron mobility transistor layers grown on 150 mm diameter Si (111) substrate. *J. Appl. Phys.* **113**, 023510 (2013).
43. Kisielowski, C. *et al.* Strain-related phenomena in GaN thin films. *Phys. Rev. B* **54**, 17745–17753 (1996).
44. Polian, A., Grimsditch, M. & Grzegory, I. Elastic constants of gallium nitride. *J. Appl. Phys.* **79**, 3343 (1998).
45. McNeil, L. E., Grimsditch, M. & French, R. H. Vibrational Spectroscopy of Aluminum Nitride. *J. Am. Ceram. Soc.* **76**, 1132–1136 (1993).
46. Yun, F. *et al.* Energy band bowing parameter in $\text{Al}_x\text{Ga}_{1-x}\text{N}$ alloys. *J. Appl. Phys.* **92**, 4837–4839 (2002).
47. Perry, W. G., Bremser, M., Zheleva, T., Linthicum, K. & Davis, R. Biaxial strain in $\text{Al}_x\text{Ga}_{1-x}\text{N}/\text{GaN}$ layers deposited on 6H-SiC. *Thin Solid Films* **324**, 107–114 (1998).
48. Davydov, V. Y. *et al.* Composition dependence of optical phonon energies and Raman line broadening in hexagonal $\text{Al}_x\text{Ga}_{1-x}\text{N}$ alloys. *Phys. Rev. B* **65**, 125203 (2002).
49. Harima, H. Properties of GaN and related compounds studied by means of Raman scattering. *J. Phys. Condens. Matter* **14**, R967–R993 (2002).
50. Grille, H., Schnittler, C. & Bechstedt, F. Phonons in ternary group-III nitride alloys. *Phys. Rev. B* **61**, 6091–6105 (2000).

Acknowledgements

The authors at Purdue University are grateful for the financial supports from National Science Foundation CAREER program (under Grants of CMMI – 1560834) and NSF IIP- 1700628. The authors thank Professor Yong P. Chen at Purdue University for allowing the use of Raman spectroscopy equipment in his lab. This research used resources of the Advanced Photon Source, a U.S. Department of Energy (DOE) Office of Science User Facility operated for the DOE Office of Science by Argonne National Laboratory under Contract No. DE-AC02-06CH11357.

Author Contributions

N.L. and I.F. contributed to the conception and design of experiments. Y.F., V.S., T.C. and B.K., conducted most of experiments, characterization and drafted the manuscript. Y.D. and H.Z. conducted synchrotron and reciprocal space mapping. N.L., I.F. and H.Z. edited and revised the manuscript. N.L. and I.F. supervised the project. All the authors discussed the results.

Additional Information

Competing Interests: The authors declare no competing interests.

Publisher's note: Springer Nature remains neutral with regard to jurisdictional claims in published maps and institutional affiliations.



Open Access This article is licensed under a Creative Commons Attribution 4.0 International License, which permits use, sharing, adaptation, distribution and reproduction in any medium or format, as long as you give appropriate credit to the original author(s) and the source, provide a link to the Creative Commons license, and indicate if changes were made. The images or other third party material in this article are included in the article's Creative Commons license, unless indicated otherwise in a credit line to the material. If material is not included in the article's Creative Commons license and your intended use is not permitted by statutory regulation or exceeds the permitted use, you will need to obtain permission directly from the copyright holder. To view a copy of this license, visit <http://creativecommons.org/licenses/by/4.0/>.

© The Author(s) 2019